Microsatellite Star Tracker Baffles: Validation and Testing

Martin Marciniak, John Enright
Department of Aerospace Engineering, Ryerson University
350 Victoria St, Toronto, Ontario, M5B 2K3; 416-979-5000(x4973/4174)
martin.marciniak@ryerson.ca,jenright@ryerson.ca

Doug Sinclair
Sinclair Interplanetary
268 Claremont St. Toronto, Canada; 647-286-3761
dns@sinclairinterplanetary.com

Tom Dzamba
Department of Aerospace Engineering, Ryerson University
350 Victoria St, Toronto, Ontario, M5B 2K3; 416-979-5000(x4973)
tdzamba@ryerson.ca

ABSTRACT

In this paper, we examine the challenges of ground-based stray light testing from a microsatellite perspective. We consider some of the historical approaches to simulation and laboratory testing and propose strategies for ground validation that require only modest investment in test facilities. The star tracker or instrument is characterized in the lab without any baffle, using a novel technique to subtract out reflections internal to the test chamber. From the resulting data a simulation element is produced, and placed at the exit of the baffle in a non-sequential ray tracing analysis. This hybrid experimental/simulation approach makes attenuation predictions that span about nine orders of magnitude, and is effective for predicting solar exclusion angles for devices that observe bright stellar targets (i.e., magnitude six or less).

INTRODUCTION

Small satellites with high performance ACS must devote precious resources to star tracker baffles. Baffles consume volume and surface area, competing with the power, thermal and communication subsystems. Little spacecraft are affected disproportionately — there is no physical reason for their baffles to be any smaller than those of a larger satellite. The system architect will want to reduce the baffle size to the bare minimum to meet the mission sun avoidance angle requirement. To do this, it is critical that a candidate baffle's actual performance be determined accurately. Small satellite star trackers have only been available for the past several years, so at this time there are few heritage baffles available.

Modern optical engineering software provides a number of tools to help engineers design and analyze baffles. Popular packages such as Zemax[1], FRED[2], and ASAP[3] are equipped with non-sequential ray-tracing engines as well as special-purpose design modules designed to facilitate stray light analysis. These packages will model a wide rage of effects including:

- Multiple reflections within the optical components (e.g., ghosting). These effects are most pronounced when the sun is close quite close to the FOV. They become less important as the source moves further off-axis.
- Unobstructed paths (e.g, 'straight-shots' through a reflecting telescope). Not usually important in simple baffles where no edges and surfaces lie within the FOV.
- Surface and volumetric scattering. These are one of the more important effects to model for star trackers.
- Self-emission. This is not relevant at optical wavelengths.
- Diffraction. Depending on the baffle design, diffraction can sometimes contribute appreciable amounts

of stray light.

Of these phenomena, scattering typically has the largest effect on stray light performance for star trackers. Optical defects — e.g., striations, voids and tiny scratches — can cause scattering in refractive elements. The reflective properties of baffle surfaces and knife edges are also vital to estimating stray light performance. Many surfaces are neither perfectly specular nor Lambertian, so most optical engineering software allows users to specify bi-directional reflection functions (BDRFs). Although this is a useful feature, it is of limited utility if the surface properties are not well-characterized. Additionally, the presence of contaminants such as dust on the refractive and baffle surfaces can make actual device behaviour difficult to predict. These limitations suggest that optical engineering software can provide relative performance estimates during baffle design, but may not be entirely accurate for validating sensor performance. Experimental validation is required to get good confidence in the on-orbit function.

In this paper we propose an approach to baffle development that requires only modest test infrastructure. Building on an approach suggested by Arnoux[4], we measure the off-axis response of the star tracker without a baffle installed. Although this black-box characterization oversimplifies the spatial response of the optics, it removes the need to have precise optical models of the lens system (e.g., As could be the case with the use of a COTS lens assembly.) and the interior surfaces of the star tracker. We have greater confidence in these results than using ray-tracing alone. The stray light model of the lens system can be used during baffle design, but also in the verification of exclusion angles and other system specifications. Unfortunately, at time of writing, we are unable to demonstrate the full integration of the two techniques. Instead we present as our main contributions: a survey of past testing strategies; detailed results from our optical calibration; and a sketch of techniques for integrating ray-tracing and laboratory testing.

The ST-16 Star Tracker

The methods presented here should be applicable to most small satellite star trackers, provided the baffle can be removed. We used an ST-16 device as the test bed to develop the experimental technique. The ST-16 is notable in that it uses a commercial lens assembly for which detailed prescription data is not available. Its stray light performance must be determined empirically as we do not have a model to ray-trace. The ST-16 has been described in previous papers[5,6]. Its key parameters are shown in Table 1.

Table 1: ST-16 Parameters

Optics design	Refracting, 4 glass elements, one aspherical
Focal length	$16\,\mathrm{mm}$
Relative aperture	$f/1.2$
Field of View	$7.5\,\mathrm{deg.}$,half-cone
Detector	CMOS active pixel sensor, 5 megapixel, $2.2\,\mu\mathrm{m}$ square pixel size

Table 2: Comparison of Sun and Star Flux

Source	Apparent Magnitude	Relative Magnitude	Relative Brightness
Target Star	6.0	0	1.0
Full Moon from LEO	-12.7	-18.7	3.0×10^7
Sun from LEO	-26.7	-32.7	1.2×10^{13}

Stray Light and Instrument Design

Star trackers use baffles to control stray light from the sun, moon, and bright Earth. There are many different Earth illumination conditions possible, so here we will consider only the sun and full moon in comparison to a typical target star (Table 2). A magnitude 6 star is visible to the human eye under good viewing conditions. There are almost 5000 such stars in the sky.

We can define the attenuation of a baffle by:

$$A_b(\theta) = \frac{\Phi(\theta)}{\Phi(0)} \tag{1}$$

where $\Phi(0)$ is the integrated flux on the detector with the sun or moon located on the boresight, and $\Phi(\theta)$ being the integrated flux with the source at angle theta from the boresight.

Our target stars will be focused onto the detector, and will illuminate a small number of pixels according to the optics Point Spread Function (PSF). Stray light from the moon and sun will cover all of the detector. For now, let us make the simplifying assumption that stray light is a uniform background across the entire detector with equal value at each pixel.

The off-axis light that reaches the detector will is attenuated by the response of both the baffle and the sensor optics. Although it is not strictly rigourous, we can of a

Table 3: Attenuation Targets

Pixels illuminated by star	20
Total pixels in detector	5000000
A_s required to match star signal to lunar background	1.2×10^{-2}
A_s required to match star signal to solar background	4.8×10^{-7}

light ray being attenuated in two steps:

$$A_s = A_b \cdot A_L \tag{2}$$

where A_s is the net system attenuation, A_b is the contribution from the baffle, and A_L the response from the sensor optics.

Table 3 shows the calculated equivalent fluxes. The table assumes PSF and detector parameters from the ST-16, which may be seen as typical for modern small star trackers. No account is made for vehicle angular motion which will introduce stellar blurring.

A uniform background will have two negative effects:

- Stray light photons will add shot noise to the image, making it harder to detect stars even when a constant value has been subtracted.
- An elevated background will push the detector towards saturation. To prevent this the exposure length must be reduced. This will further decrease the stellar signal relative to the shot noise.

The actual stray light image may be non-uniform, with certain areas of the detector receiving more illumination than others. If there is fine structure to the background there may be persistent features that can be mistaken for stars.

If $A_s(\theta)$ is such that the star signal is much brighter than the background, it is clear that the star tracker will function correctly. The exact boundary for stellar detection against a stray light has not yet been explored. As a placeholder, we will assume that $A_s(\theta) = 10^{-8}$ is sufficient for robust rejection of sunlight at modest vehicle rates.

Stray Light Testing Techniques

The challenges of stray light testing have been recognized for some time and engineers have developed a number of clever techniques to advance the capabilities of ground-based experiments. Our contributions are not dramatically different from prior approaches. Instead, we present a discussion of previous techniques and a pragmatic reference approach that gives good measurement capabilities using modest test facilities.

The fundamental problem with ground-based stray light testing is the difficulty in replicating realistic illumination characteristics: i.e., very bright off-axis illumination with a comparatively dim scene in the field of view. Many factors in ground tests introduce extra photons to the detector that would not present on-orbit. This raises the level of background illumination and underestimates the performance of the baffle. Schenkel[7] provides an early description of the difficulties involved in stray light measurement. Indoor lab tests typically struggle with finding an appropriate beam dump (both direct and reflected from the sensor) so that the beam doesn't end up lighting up the walls that lie in the FOV. Bock, et al[8], avoid this problem by moving their test setup outdoors. Without enclosing walls, the off-axis beam can be easily dumped to empty space. The success of this approach depends on the quality of local seeing conditions and the ease with which the experimental facility can be adapted.

All tests in atmosphere must contend with light scattered from the illuminated air volume that lies within the field of view. Kemp and Wyatt[9] make a detailed study of this phenomenon. They show how a clean facility (i.e., with filtered air) can improve the background illumination by minimizing Mie scattering; Rayleigh scattering cannot be avoided but contributes less to the background illumination.

Beam design and management is a critical part of any stray light test facility. A typical setup includes a motorized test stand that orients the sensor and baffle within the beam of a sun-simulator lamp. Kilowatt-class Xenon arc-lamps are the favoured solution for optical-frequency testing[10,11] but halogen lamps can also be used, particularly in the near-infrared[12,8]. These large lamps are collimated to produce sizable beams ($25-35$ cm). Large beams offer good spatial uniformity but increase the scattering volume within the sensor FOV. Keeping the illumination close to AM0 intensity reduces the need to adjust the sensor gain or exposure time during off-axis measurements, but necessitates significant investment in infrastructure. The lab surrounding the lamp and test stand must also be carefully designed. Kemp and Wyatt[12] describe a black, specular test-chamber shroud to help manage indirect beam illumination; Kawano, *et al.*[13], employ an elaborate beam dump to control reflected light.

The relevant figure of merit when discussing stray light test facilities is the attenuation factor $A_s(\theta)$ between the on-axis and off-axis illumination. Put another way, the

sun exclusion angle can be defined by the angle at which the A_s is small enough that stray light will not affect the proper functioning of the instrument. Any facility or set of test techniques will have a lower bound on the smallest value of A that can be measured before noise and background illumination dominate. The intended use of the instrument under test will determine the necessary value of A_s. For example a star tracker, observing fairly bright stars (i.e, brighter than magnitude 6.0), may need to demonstrate that $A_s = 10^{-9}$, but a more sensitive instruments studying zodiacal light may require $A_s = 10^{-15}$ [14].

No reported test facilities can provide a dark enough background to measure this range of attenuation directly. A number of techniques have been developed over the years that allow the experimenter to measure relative attenuation, and with some careful accounting, estimate the net effect. Leinart and Kluppelberg [14] suggest a number of techniques to individually characterize the elements of a complete instrument (e.g., refractive elements, baffle surfaces, knife edges), and then combine the results. Kemp and Wyatt [9] separate the contributions of each baffle vane by artificially extending the sensor field of view. Bock, *et al.* [8], physically test one section of their baffle at a time and build up a composite estimate of the overall performance. They also subtract background and scattered light by introducing a blocking vane into the beam. This has little effect on the scattering volume but eliminates any contributions from the beam striking the baffle and optics. The laboratory testing techniques that we employ in this paper are quite similar to their approach.

STRAY LIGHT CHARACTERIZATION.

Our primary goal in this paper is to suggest approaches to evaluating the stray light performance of star trackers and their baffles. This type of testing is often a challenge. As discussed earlier, many installations use very large sun-simulators and purpose-built lab facilities. For universities and smaller manufacturers, these resources may not be available. In contrast, we propose a more modest test facility and concentrate on characterizing the sensor alone without the baffle installed. This decision complicates the interpretation of the test results, but allows us to make do with a smaller lamp and narrower test beam.

The SAIL Test Facility

Laboratory tests for this study were conducted at the Space Avionics and Instrumentation Laboratory at Ryerson University. The sensor was attached to a motorized gimbal, used to orient the sensor. Simulated sun illumination was produced by a $75\,\mathrm{W}$ Xenon arc-lamp. The light source was coupled to an integrating sphere and collimated to produce a uniform beam approximately $8\,\mathrm{cm}$ in diameter. As the test platform rotates the sun lamp moves in the direction defined by the rows on the image detector.

To minimize background illumination within the field of view, it is important to pay attention to the interior of the test chamber. Indicator LEDs on the outside and inside of computer chassis, light leakage from LCD backlights (even when blanked) and stray illumination from the beam lamp can all produce significant ambient illumination. These sources must be masked when possible or separated from surfaces within the FOV with opaque screens.

Measurement Procedure

Detailed in this chapter is a procedure that when performed will estimate the point source response function for a sensor. This procedure can be performed with or without a baffle, either to observe the lens only response or to validate ray tracing predictions. Figure 1 provides a general idea of the decision making and flow of the stray light testing procedure. This will serve as a reference template as each action is explained. The experiments consist of taking images with a sensor starting with the light beam aligned with the boresight and afterwards increasing the offset angle (θ) between the two axes using fixed steps until some arbitrary ending angle sufficiently far away; at each angle an image is taken. The SAIL tests used an offset angle range between 0° and 45°.

There are two regions of angles that are of interest. The ranges of angles that the beam is directly identified within the FOV of the image will be referred to as 'on-axis', similarly the angles outside of this subset will be referred to as 'off-axis' angles.

We define that a useful image is obtained from the sensor when it satisfies the following criteria. The sensor must be exposed for long enough to clearly see any features of the light beam entering the sensor. However, it is important that no pixel is in a saturated state otherwise information loss occurs. Therefore a successful image is obtained when the exposure time ($t_{\exp}(\theta)$) is increased to the point where the image is just under the saturation level. To reduce noise it is useful to take several consecutive images and average each individual pixel across all of the images. Due to interface bandwidth constraints with the ST-16, we do not download full-frame images. Instead we sample 14 complete rows, sampled in pairs across the image. For simplicity we shall continue to refer to these as 'images'. It may also occur that several individual pixels may saturate randomly (specifically for images with longer exposure times) so it may be useful to spatially smooth the

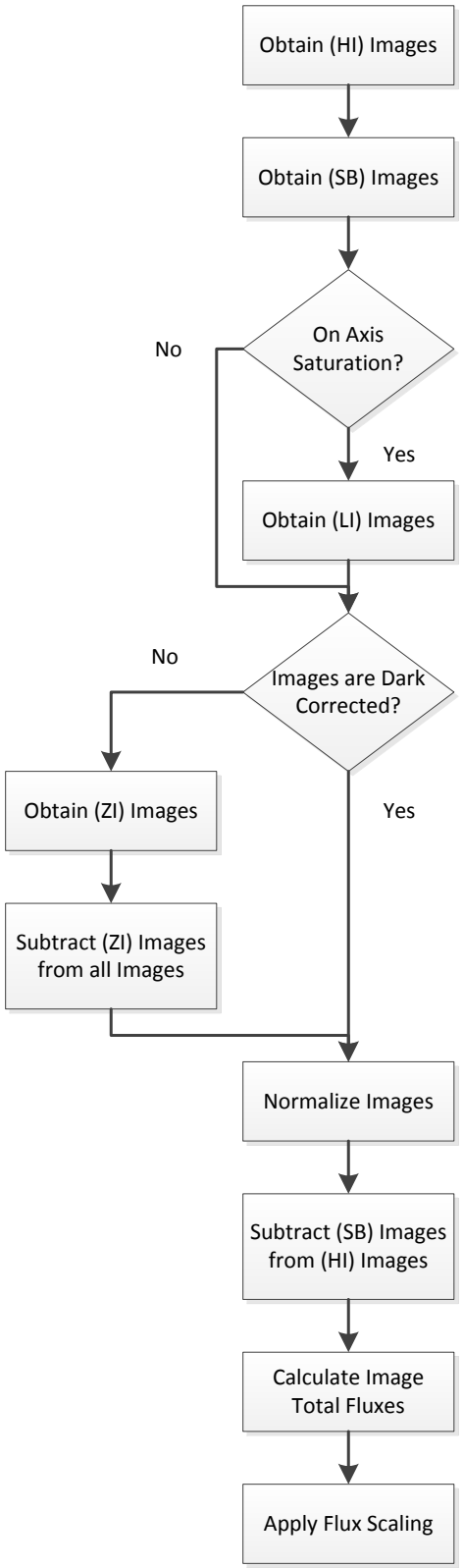

Figure 1: Overview of the Stray Light Test.

image itself using a neighbourhood averaging filter. This is to ensure that saturation is likely to be caused by the light response rather than a thermal response. The SAIL tests used 3 consecutive images to reduce temporal noise, as well as used a simple neighbourhood average filter that averaged three row pixels (including the target and the two adjacent pixels on each side) to reduce thermally induced saturation.

There will be three different types of rays entering the sensor at any given time (see Figure 2a). The first type is attributed to direct photons. These are photons that start at the source, scatter off baffle or lens surfaces, and terminate within the sensor. This is the subset of light that is desired to be isolated using the tailored experiments, these rays will generate the more intense off-axis phenomena because they experience the least amount of attenuation.

The second type of light is that attributed to scattered rays. These are the rays that hit particles or molecules within the volume of air in front of the sensor and trigger the Rayleigh or Mie scattering phenomena. The third type is due to ambient rays. These are attributed to residual reflections off of surfaces within the environment or overlooked light sources. Both scattered and ambient rays contribute to masking the true response of the sensor to direct light as it would be in the vacuum of space.

Depending on sensor hardware being used there will be additional unwanted signal sources that will corrupt the direct light as well. Charged-couple devices (CCDs) experience a phenomena called "dark current" in which over longer exposure times, an additional signal accumulates that is independent of signals generated due to the sensor being exposed to light.

We wish to isolate the direct light that generates the true point source response function for sensor. This is performed by utilizing two experiments that when combined will yield an estimate of the pure off-axis response to the direct light.

Figure 2a shows the sensor exposed to the full beam configuration and shows the different types of light that will enter the sensor with that configuration. The purpose of this configuration is to obtain the off-axis response for the sensor. The light entering the sensor for this test is a combination of all three types of rays simultaneously in addition to noise. The light source for this configuration must be at its maximum intensity setting because any off-axis observation is much dimmer than an on-axis counterpart.

Figure 2b on the other hand, shows the masked beam configuration. This objective of this configuration is to block the direct beam to the sensor in order to gauge the back-

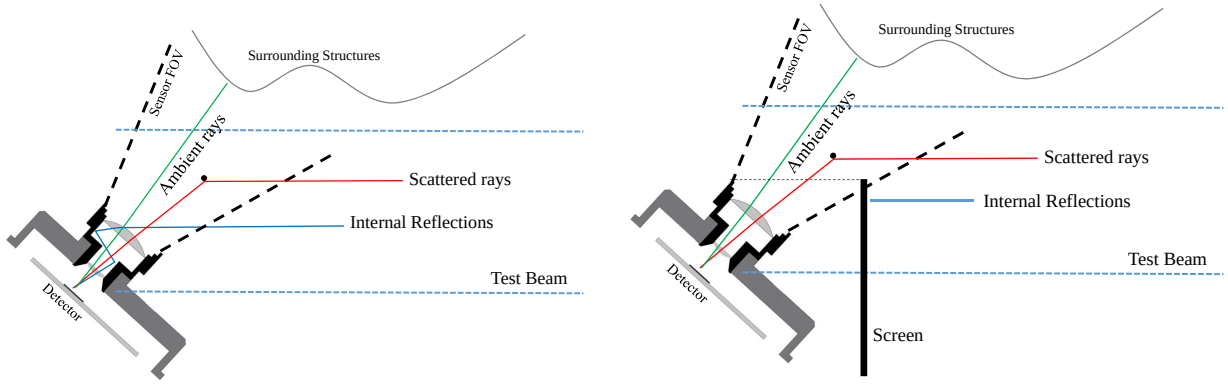

(a) Full beam configuration.

(b) Direct beam blocked by screen.

Figure 2: Beam testing approach

ground light. The background light consists of the scattered rays and the ambient rays as well as any additional noise.

Combining all of these results, we can perform a series of operations to deduce the approximate off-axis response for the sensor. Depending on the hardware utilized there are some additionally required data in order to obtained the entire point source response. We will cover these additional data requirements shortly.

There are a total of four different data acquisition tests that are needed to gain sufficient insight into the off-axis light response of the sensor. These several configurations are listed below. We will use the subscript notation enclosed in the parentheses to distinguish between the data sets.

1. A high intensity source (see Figure 2a) with the full offset angle range. (HI)
2. A semi-blocked high intensity source (see Figure 2b) with the off-axis angle range only. (SB)
3. A low intensity source with the on-axis angle range including the first five angles of the off-axis range. (LI)
4. A completely dark room (zero illumination), using the exposure times of the other data sets. (ZI)

At each off-axis angle, θ we acquire a processed image to reduce noise. We denote the image as $\mathbf{I}(i,j)$ where i and j are the row and column indices, respectively. As part of the imaging process in the HI test, we adjust the sensor exposure time, $t_{\exp}(\theta)$, to produce a high, but non-saturated peak intensity over $\mathbf{I}$. The peak intensity is $I_{\max}$.

The purpose of the first two experiments were discussed previously; together they are used to isolate the direct light entering the sensor. The purpose of the third experiment is dictated by hardware limitations. It is difficult to obtain a full useful range of data in terms of a combined set of on-axis and off-axis responses. The reason being that the difference in magnitude between on-axis and off-axis light is very significant; for example, a suitable light source for the off-axis illumination is often unsuitable for on-axis data because it will saturate the pixels on the sensor even on the minimum exposure time setting. Likewise, a suitable on-axis light source is too dim to observe any useful off-axis response. The goal of the third experiment is to obtain insight into the border between on-axis behaviour and off-axis behaviour. These results are used to estimate and expand the first experiment's results for the full range of angles if needed.

The dark tests are used to dark correct the other data sets. Some dark correction can be performed during the image acquisition process; if the sensor's active pixel area is smaller than the whole sensor then for a given image there will be information on the dark background within the border surrounding the active region. This information can be used to calculate pixel offsets without the need to take a zero illumination image. We will proceed assuming that this is not the case and will discuss dark correction using a conventional method.

To dark correct (DC) a desired image, the dark image is subtracted from the exposed image; both images must share a common exposure time. For example, to correct the images from the first experiment we would perform the following operations.

$$\mathbf{I}_{\mathrm{HIDC}}(i,j) = \mathbf{I}_{\mathrm{HI}}(i,j) - \mathbf{I}_{\mathrm{ZI}}(i,j) \tag{3}$$

Likewise the same operation would be performed on the other sets of images as well. It is important to dark correct the images before performing any further operations because it distinguishes actual light responses from pixel offsets. Light response scales with exposure times, but pixel offsets remain primarily time independent which is important during image normalization. A sample normalization would be:

$$\mathbf{T}_{\mathrm{HIDC}}(i,j) = \frac{\mathbf{I}_{\mathrm{HIDC}}(i,j)}{t_{\mathrm{exp}}(\theta)} \tag{4}$$

In order to completely isolate for the direct light (DL) entering the sensor, one must subtract out the semi-blocked images from the fully illuminated images; subtracting the images simply removes ambient information. Two images can only be subtracted in this case if they refer to the same physical orientation in space (i.e. possess the same orientation angle). The images may have different exposure times but this is taken into account when the images are normalized by exposure time. To extract the direct light information from the fully illuminated images, we would perform:

$$\mathbf{T}_{\mathrm{DL}}(i,j) = \mathbf{T}_{\mathrm{HIDC}}(i,j) - \mathbf{T}_{\mathrm{SBDC}}(i,j) \tag{5}$$

Note that (5) is only valid for the off-axis angle range.

To quantify the degree of light entering the sensor, we define the total flux quantity for a given image. We first normalize the image with respect to its exposure time, then the row-wise sums are calculated and averaged amongst all of the rows within the image. For instance, the average direct light flux, Φ_{DL}, is:

$$\Phi_{\mathrm{DL}}(\theta) = \frac{1}{n_{\mathrm{rows}}} \sum_{i=1}^{n_{\mathrm{rows}}} \sum_{j=1}^{n_{\mathrm{cols}}} \mathbf{T}_{\mathrm{DL}}(i,j) \tag{6}$$

This same quantity can be calculated for the other sets of images as well.

Should saturation occur for the on-axis portion of the first data set, the true total flux of the images will be significantly higher than the ones obtained using (6). The true total flux can be estimated using the third data set (LI).

The total flux varies over a large range as the star tracker rotates away from the beam. Due to limitations of the sensor hardware it may not be possible to vary t_{exp} over a wide enough range to preserve a good signal to noise ratio at all the tested θ angles. In this case the raw intensity of the beam can be adjusted using neutral density (ND) filters — i.e., high index filters close to the beam, and low index filters further away from it. In order to reconcile a common scale for the all of the off-axis angles, we must calculate additional scaling terms when we change the beam intensity. To illustrate this technique, consider the following scenario.

At a certain angle θ_{lim}, we near the upper bound on exposure time, i.e., $t_{\mathrm{exp}} = t_{k-}$ and collect the low intensity flux measurement $\Phi_1(\theta_{lim},\, t_{k-})$. We then change the ND filter to reduce the beam attenuation and then repeat the measurement. The new exposure time is then $t_{\mathrm{exp}} = t_{k+}$ and the flux is $\Phi_2(\theta_{lim},\, t_{+})$. Correcting for this intensity change means that subsequent flux measurements must be multiplied by the relative scaling factor:

$$b_k = \frac{\Phi_1(\theta_{\mathrm{lim}},\, t_{k-})}{\Phi_2(\theta_{\mathrm{lim}},\, t_{k+})} \tag{7}$$

For sample points where we do not adjust the beam intensity we can assume a relative scaling factor of unity.

Thus we can rewrite (6) to incorporate the global intensity scaling as well as the LI measurements to replace the HI saturated measurements:

$$\Phi_{\mathrm{DL}}(\theta_k) = \begin{cases} B_k \Phi_{\mathrm{LIDC}}(i,j), & \text{if } \theta_k < \theta_{\mathrm{lim}} \\ B_k \Phi_{\mathrm{DL}}(i,j), & \text{if } \theta_k \geq \theta_{\mathrm{lim}} \end{cases} \tag{8}$$

where

$$B_k = \prod_{s=1}^{k} b_s \tag{9}$$

Once we have collected a full set of Φ_{DL} measurements, we can normalize the flux to find the attenuation factor $A_L(\theta)$:

$$A_L(\theta_k) = \frac{\Phi_{\mathrm{DL}}(\theta_k)}{\Phi_{\mathrm{DL}}(0)} \tag{10}$$

As long as the flux response is sufficiently strong, we can make good measurements of the off-axis lens response. However, at some point, increasing noise makes further attenuation difficult. We must therefore define a threshold to decide where the flux levels are trustworthy.

We look to the dark images for the noise information required. The dark images can be broken down into their components:

$$\mathbf{I}_{\mathrm{ZI}}(i,j) = f\left(\ \mu(i,j),\quad \sigma(i,j)\ \right) \tag{11}$$

Where μ denotes a mean pixel value and σ refers to the pixel standard deviation from the mean.

The noise distribution can be found using several methods, a distribution can be analyzed over the entire image, the rows individually, or even across the sensor Bayer pattern itself. The distribution for the tests presented were calculated using a Bayer pattern of known size 2×4 that repeated across the entire image for each pair of rows. The standard deviations were calculated for each individual pixel in the pattern using the knowledge of the entire pair of rows. Therefore a standard deviation value can be assigned to each individual pixel in the image as in (11).

The dark correction of the images indirectly subtracted the means of each pixel but still preserved noise distribution. To trust our calculated flux levels we require a conservative noise threshold to compare with. A 3σ confidence level can be calculated for each individual pixel which is then used to generate a flux level similarly to (6). The noise fluxes are then normalized by their exposure time to exist on a common scale with the other flux values. The 3σ upper limit for the noise flux is calculated as:

$$N_{ZI} = \frac{3}{\sqrt{n}}\Phi_{\sigma}(t_{\mathrm{exp}}) \tag{12}$$

Where Φ_{σ} refers to the flux generated from an image where each pixel value is equal to the standard deviation for that pixel's distribution (i.e., $\mathbf{I}_{\sigma}(i,j) = \sigma(i,j)$), and n refers to the number of pixels used to generate the distributions. For example, if the distribution was generated with all of the pixels along a row then $n = n_{\mathrm{cols}}$. For our analysis using the Bayer patterns, we used the number of Bayer patterns per pair of rows which translates to $n = n_{\mathrm{pattern}}$.

Below this noise threshold level, it is difficult to distinguish between dark noise and low intensity flux. It is important to note that the noise flux threshold is valid for the direct light flux that shares the same exposure time.

Figure 3 plots the results of (10) and the noise flux levels of (12) (normalized by Φ_{DL}) paired to the DL exposure times. This figure gives an overview of the attenuation throughout the complete angle range along with the noise floor for these values. Here one can observe the characteristics of the complete point response function and how

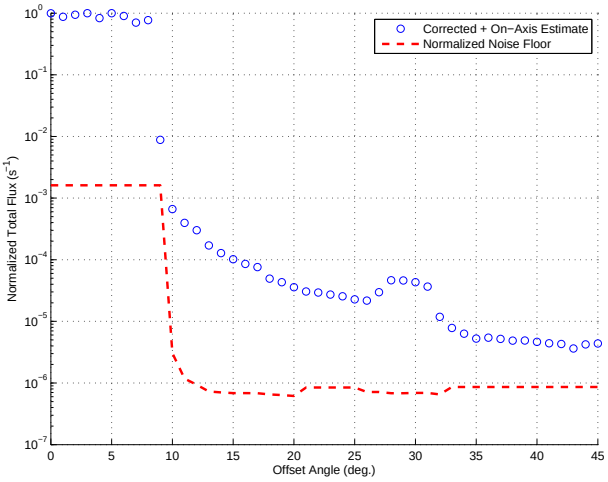

Figure 3: Off-axis performance attenuation measurements.

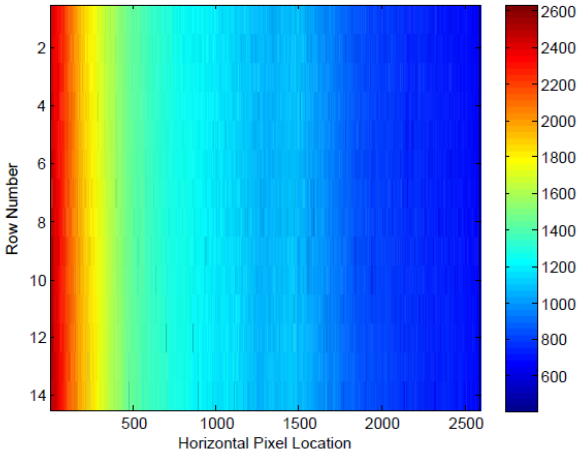

Figure 4: Sample direct light image at 17° as obtain through the procedure.

it manifests itself as a total flux value. This presentation of the data permits the baffle designer to clearly see areas of interest for the equipment. For instance in our tests for the ST-16 sensor, we see a strange illumination increase throughout the $26° - 31°$ range which is likely due to a prevalent internal reflection occuring. Baffle design for this sensor would obviously aim to remove this behaviour. The difference in illumination levels from on-axis to just off-axis is on the order of 10^3 and it can clearly be observed that the total illumination decays with an increasing offset angle.

Another interesting relationship found is that for offset angles beyond the on-axis angle range, the illumination gradient within each image is primarily one dimensional

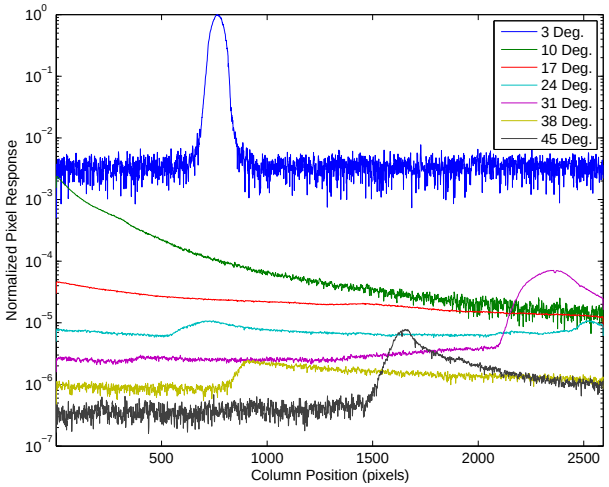

Figure 5: Spatial variation of stray light.

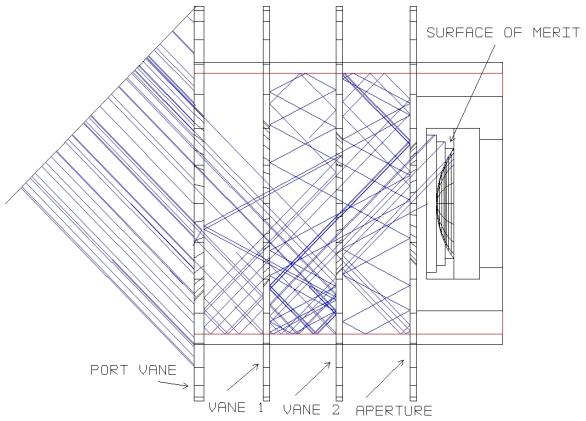

Figure 6: A ray trace example.[15] .

in nature. Figure 4 shows a visualization of a direct light image (DL) at an offset angle of $17°$. One can clearly see that each sampled row pair is very similar to the others. This is not a normalized image, it was obtained with an exposure time $t_{\text{exp}} = 2.5868$ seconds and the saturation value for the ST-16 is at 4095 which demonstrates the dimness of the gradient for this offset angle. Local gradients between consecutive pairs of rows were similar for the majority of the off-axis angle range. By averaging the sensor values between all the rows in an image, the spatial variations can be distinguished without the need of interpreting color data.

Figure 5 shows the spatial variations sampled at regular angle intervals. The initial light beam maximum starts at the centre of the image and then proceeds to travel to the left as the offset angle is increased. As the beam travels further off-axis, some much dimmer maxima begin to occur. These are speculated to be internal reflections within the sensor itself. It is worth noting that the strongest of the dimmer maximum lies alongside to the interesting 'hump' within Figure 3.

RAY TRACING

Using optical engineering software for ray-tracing is a standard approach to stray light analysis. Non-sequential ray tracing engines are necessary to account for multiple reflections off of arbitrary surfaces. In this section, we sketch our approach to integrating ray-tracing with laboratory characterization.

Stray light analysis begins by setting up the reference geometry for the baffle. This includes the optical FOV; the number, length, and placement of vanes; and surface properties insofar as they are known. During baffle design it is often convenient to express the geometry in terms of parametric constraints to facilitate optimization — for instance the maximum vane length can be determined by its position in order to keep the knife edge just outside of the FOV. Light sources must be set up to illuminate the whole entrance aperture.

Figure 6 shows a simple example of this sort of analysis. Solver options such as importance sampling can be used to reduce the required number of rays and increase the solution speed. The energy in the rays hitting the surface of merit — frequently the front lens element or merely the exit port of the baffle — count toward the A_b calculations.

Summation of the rays reaching the surface of merit gives an initial estimate of the baffle performance (Figure 7). Conducting this analysis close to boresight is of limited value since direct rays striking the lens surface will dominate the response. It is difficult to use this initial analysis to estimate exclusion angles and other metrics. This is because the analysis does not capture the response of the optical system itself. None of the rays striking the lens surface arrive at angles less than the FOV dimension, so internal attenuation will play a large role in system performance. If the detailed optical system design is available, it can be integrated into the analysis, but if the lens assembly is a COTS product, its behaviour must be characterized with laboratory testing.

Laboratory testing results provide the response of the system, A_L, as a function of off-axis angle, θ The ray arrival angle will affect its transmission to the detector. Thus, we cannot merely multiply the curves from Figure 3 and Figure 7 to get the total system attenuation. Instead $A_L\,(\theta)$ can be used to weight the rays emerging from the baffle based on the angle with which they cross the exit port.

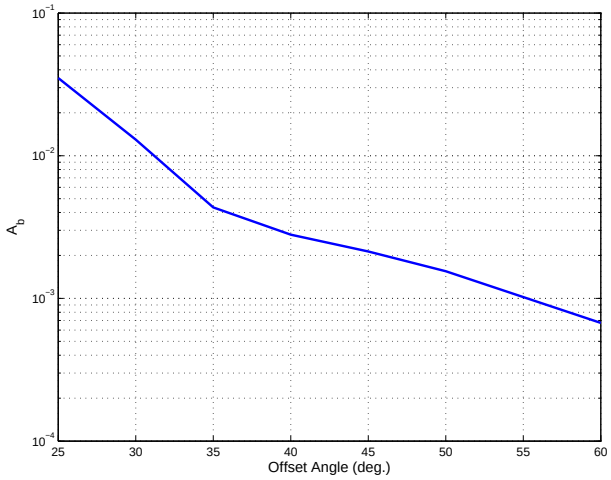

Figure 7: Predicted baffle attenuation (adapted from [15]).

The lens testing results measure attenuation across more than five orders of magnitude and the baffle ray tracing makes predictions over more than three. We expect that the combined analysis should give measurement results over the range of 10^{-8} to 10^{-9} which we we expect to be sufficient to determine sun exclusion angles. Although we have not been able to complete this analysis at time of writing, we feel that this approach is sound. Further tests are planned to try and assess the relative importance of incidence angle and incidence position.

CONCLUSIONS

This paper presents a practical solution for stray light testing within atmosphere. Using modest laboratory infrastructure we are able to characterize the off-axis response of a star tracker lens. We have also outlined several strategies for combining this analysis with ray tracing to permit baffle design and performance verification. Unlike similar testing strategies, our approach does not require large sun-simulator lamps or extensive modifications to the our test facilities, beyond thorough management of stray light.

Delays encountered during laboratory testing prevented us from integrating the lens and baffle analyses. The range of attenuation observed in these two techniques, and our understanding of the detection capabilities of our star tracker, strongly suggest that our approach will provide good quality estimates of exclusion angles. Completing this integration is our near term goal. Follow-on studies will validate the predictions arising from the completed analysis. Lunar exclusion angles can be validated with night sky testing, solar exclusion angles will require on-orbit data or a test campaign at a larger facility.

We are optimistic that this two part technique will be a useful technology for the small satellite community. It offers potential benefits during both design and validation phases of star tracker development. If the technique can be further improved, it might also be applied to small science instruments as well.

References

1. Zemax, "Advanced Path Analysis," `http://www.radiantzemax.com/zemax/features/advanced-path-analysis`, Accessed June 2013.

2. Photon Engineering, "FRED Stray Light Application Note," `http://www.photonengr.com/files/2010/10/ApplicationNote_StrayLight.pdf`, October 2010.

3. Breault Inc., "Stray Light Analysis in ASAP (BROPN1157)," `http://www.breault.com/resources/kbasePDF/bropn1157_straylight.pdf`, May 2013.

4. Arnoux, J.-J. P., "Star sensor baffle optimization: some helpful practical design rules," 1996.

5. Enright, J., Sinclair, D., Grant, C. C., Dzamba, T., and McVittie, G., "Towards Star Tracker Only Attitude Estimation," *Proc. of the 24th AIAA/USU Conference on Small Satellites*, Logan, Utah, Aug. 2010.

6. Enright, J., Sinclair, D., and Dzamba, T., "The Things You CanŠt Ignore: Evolving a Sub-Arcsecond Star Tracker," *Proc. of the 26th AIAA/USU Conference on Small SatellitesProc. of the 24th AIAA/USU Conference on Small Satellites, SSC12-X-7*, Vol. SSC12-X-7, Logan, Utah, Aug. 2012.

7. Schenkel, F. W., "An automatic self deployable high attenuation light shade for spaceborne sensors," *Journal of the British Interplanetary Society*, Vol. 26, 1973, pp. 589.

8. Bock, J. J., Lange, A. E., Matsuhara, H., Matsumoto, T., Onaka, T., and Sato, S., "Cooled baffle system for spaceborne infrared telescopes," *Applied optics*, Vol. 34, No. 13, 1995, pp. 2268–2277.

9. Kemp, J. C. and Wyatt, C. L., "Terrestrial Measurement of the Performance Of High-Rejection Optical Baffling Systems," *Optical Engineering*, Vol. 16, No. 4, Aug. 1977, pp. 164412–164412.

10. Kawano, H., Shimoji, H., Yoshikawa, S., Miyatake, K., Hama, K., and Nakamura, S., "Suppression of sun interference in the star sensor baffling stray light by total internal reflection," 2005.

11. Heinisch, R. P. and Jolliffe, C. L., "Light baffle attenuation measurements in the visible," *Applied optics*, Vol. 10, No. 9, 1971, pp. 2016–2020.

12. Kemp, J. C. and Wyatt, C. L., "A Specular Chamber for Off-Axis Response Evaluations of High-Rejection Optical Baffling System," Tech. rep., DTIC Document, 1976.

13. Kawano, H., Shimoji, H., Yoshikawa, S., Miyatake, K., Hama, K., and Nakamura, S., "Suppression of sun interference in the star sensor baffling stray light by total internal reflection," Sept. 2005, pp. 59621R–59621R.

14. Leinert, C. and Kluppelberg, D., "Stray light suppression in optical space experiments," *Applied Optics*, Vol. 13, No. 3, 1974, pp. 556–564.

15. Desaulniers, D.-L., "Baffle Design: Sinclair, Sail, SFL Star tracker," Tech. rep., Contractor Report, October, 2010.